

# Dilute Pd/Au Alloy Nanoparticles Embedded in Colloid-Templated Porous SiO<sub>2</sub>: Stable Au-Based Oxidation Catalysts

Mathilde Luneau,<sup>†</sup> Tanya Shirman,<sup>‡,§</sup> Amanda Filie,<sup>‡</sup> Janis Timoshenko,<sup>‡</sup> Wei Chen,<sup>||,Ⓛ</sup> Antonios Trimpalis,<sup>#</sup> Maria Flytzani-Stephanopoulos,<sup>#</sup> Efthimios Kaxiras,<sup>||</sup> Anatoly I. Frenkel,<sup>‡,∇,Ⓛ</sup> Joanna Aizenberg,<sup>†,‡,§</sup> Cynthia M. Friend,<sup>†,‡,Ⓛ</sup> and Robert J. Madix<sup>\*,‡,Ⓛ</sup>

<sup>†</sup>Department of Chemistry and Chemical Biology, <sup>‡</sup>John A. Paulson School of Engineering and Applied Sciences, <sup>§</sup>Wyss Institute for Biologically Inspired Engineering, and <sup>||</sup>Department of Physics and School of Engineering and Applied Sciences, Harvard University, Cambridge, Massachusetts 02138, United States

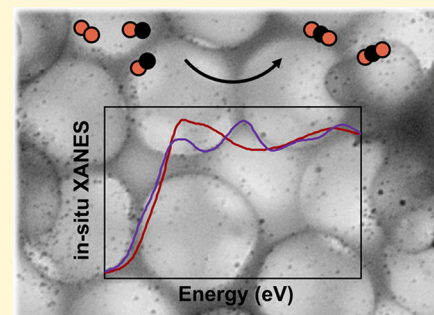
<sup>‡</sup>Department of Materials Science and Chemical Engineering, Stony Brook University, Stony Brook, New York 11794, United States

<sup>#</sup>Department of Chemical and Biological Engineering, Tufts University, Medford, Massachusetts 02155, United States

<sup>∇</sup>Chemistry Division, Brookhaven National Laboratory, Upton, New York 11973, United States

## Supporting Information

**ABSTRACT:** Dilute alloy materials hold great promise for enhancing selectivity in catalytic reactions. A major challenge with such catalytic materials is developing supported alloy nanoparticles (NPs) with a catalytically optimal composition that are stable with respect to sintering. Here, we demonstrate that NP Pd/Au catalysts with minor concentrations of Pd prepared by a colloid-templating approach are active for oxygen dissociation and catalytic oxidation, as exemplified by CO oxidation. Using electron microscopic imaging, infrared spectroscopy, and X-ray photoelectron spectroscopy, we demonstrate that Pd is stabilized within the Au nanoparticle in its metallic state with minor amounts of Pd at the surface. The Pd–Au nanoparticles are embedded in the colloidally templated silica and form a thermally stable catalyst at high temperature. Surface analysis by diffuse reflectance infrared spectroscopy indicates that the Pd atomic distribution at the surface varies with the bulk concentration, forming isolated Pd atoms at 2% Pd and a mixture of Pd monomers and small Pd clusters at 9% Pd. X-ray absorption fine structure analysis indicates that Pd is well distributed in the bulk of the nanoparticle. In-depth understanding of this new class of catalytic materials opens the way to a wide array of possibilities for crucial enhancement of activity and selectivity in catalysis.



## 1. INTRODUCTION

Au–Pd bimetallic systems show considerable promise as they have proven to be active for a wide array of catalytic reactions ranging from alcohol and alkane oxidation to hydrogenation of alkynes.<sup>1–11</sup> In particular, dilute Pd–Au alloys have raised great interest. Indeed, the presence of isolated Pd atoms in Au has shown to afford unique reactivity for acetoxylation of ethylene to vinyl acetate,<sup>12</sup> hydrogenation of cyclohexene and butadiene,<sup>11,13</sup> and, more recently, for the selective hydrogenation of 1-hexyne in the liquid phase.<sup>2</sup>

A broader question remains: can one find an optimum structure and composition that leads to stable and enhanced activity and selectivity? Determining such critical features in the case of dilute bimetallic systems is particularly challenging. Indeed, many aspects from preparation to characterization render this investigation difficult. As-prepared catalysts are oftentimes a nonhomogeneous mixture of particles of different sizes and compositions. Particles on the same catalyst have usually diverse Pd–Au compositions or can even be a mixture of Pd–Au alloys and free Au or free Pd.<sup>6–8,14</sup> In addition, the detection of highly diluted metal challenges detection limits

and requires careful analysis by cutting-edge experimental techniques. Moreover, the distribution of the two metals can be dynamic during reaction conditions.

Recently, thermally stable, dilute Ag-in-Au alloy nanoparticles that are partially embedded in a porous SiO<sub>2</sub> matrix were synthesized and utilized for highly selective coupling of alcohols to form esters.<sup>15</sup> Fine control over the composition, morphology, size, distribution, and availability of the supported nanoparticles was demonstrated. This synthetic methodology is highly customizable and can be used for the design of a wide range of catalytic systems. Here, we demonstrate the applicability of this design for diluted Pd-in-Au NPs supported on colloid-templated silica.

We develop an approach to combine spectroscopy and imaging to understand the catalytic material for a simple prototype: CO oxidation. CO oxidation is a relatively simple reaction involving first O<sub>2</sub> activation and second, the removal

Received: May 6, 2019

Revised: July 2, 2019

Published: July 10, 2019

of adsorbed O by CO. It provides a simple test of several aspects of structure sensitivity. Thus, as a probe reaction, it can provide insights into the effects of composition and structure of the active phase under different reaction conditions.

## 2. MATERIALS AND METHODS

**2.1. Material Synthesis.** Au and Pd monometallic and Au–Pd bimetallic nanoparticles with various Pd contents were synthesized.

Au nanoparticles (Au NPs) were synthesized using the modified published method.<sup>16</sup> Typically, a solution of ~5 nm Au NPs was prepared by adding 10 mg of HAuCl<sub>4</sub> to 100 mL of H<sub>2</sub>O with vigorous stirring, followed 1 min later by the addition of 1 mL of 1% aqueous trisodium citrate. After an additional minute, 1 mL of 0.075% NaBH<sub>4</sub> in 1% trisodium citrate was added. The solution was stirred for 5 min and then stored at 4 °C until needed.

Poly(vinylpyrrolidone) (PVP)-capped Pd NPs were synthesized by the NaBH<sub>4</sub> reduction of Pd(NO<sub>3</sub>)<sub>2</sub> according to published procedure with slight modification. Briefly, 4.3 g of PVP was added to 75 mL of DI water under stirring followed by the addition of 13.64 mg of Pd(NO<sub>3</sub>)<sub>2</sub>. The solution was capped in an ice bath under an Ar bubbling for 30 min under stirring, then 1.5 mL of NaBH<sub>4</sub> aqueous solution (0.5 M) was quickly added, and the reaction flask was left in the ice bath under an Ar atmosphere for additional 10 min. Then, the reaction mixture was removed from the ice bath and left for aging for 48 h without stirring (covered, room temperature).

Nanoparticles with dilute Pd content in Au were prepared using the modified published procedure.<sup>17</sup> As-prepared Au NP solution was used to synthesize the Pd<sub>x</sub>Au<sub>1-x</sub> bimetallic NPs (*x* = atomic fraction of Pd, as determined from inductively coupled plasma mass spectrometry (ICP-MS)). Typically, to 40 mL of as-synthesized Au NP solution, 5 mL of ascorbic acid aqueous solution (0.1 M) was added under stirring at room temperature. The Pd<sub>x</sub>Au<sub>1-x</sub> bimetallic NPs with various Au/Pd ratios were synthesized by the addition of certain volumes of Pd(NO<sub>3</sub>)<sub>2</sub> aqueous solution (10 mM): 60 and 150 μL for the synthesis of Pd<sub>0.02</sub>Au<sub>0.98</sub> and Pd<sub>0.09</sub>Au<sub>0.91</sub>, respectively. The reaction mixture was stirred for 12 h at room temperature and stored at 4 °C.

A templating approach previously described was used to synthesize the final catalytic materials (S1 and S2 in Supporting Information (SI)).<sup>18</sup> Briefly, composite colloids (PS@Pd<sub>x</sub>Au<sub>1-x</sub>) were synthesized by adding specific amounts of Pd<sub>x</sub>Au<sub>1-x</sub> nanoparticles to the colloidal dispersion of thiol-modified polystyrene colloids. After the formation of a colloidal assembly, a silica precursor was used to fill the interstitial space between the polystyrene spheres by capillary forces. The backfilled samples were dried and finally calcined at 500 °C in air for 2 h.

**2.2. Ex Situ Characterization Techniques.** Inductively coupled plasma mass spectrometry (ICP-MS) was used to determine the total metal loading and Au/Pd bulk ratios (Agilent Technologies 7700x). Scanning electron microscopy (SEM) and transmission electron microscopy (TEM) were used to evaluate the catalyst's structure and the nanoparticle's size distribution. Transmission electron microscopy images were acquired using a JEOL 2100 microscope (Japan) with an operating voltage of 200 kV. The samples for TEM images were made by placing a drop of the metal NP solution on a TEM carbon-coated grid. High-resolution images were taken using a Gatan Osiris digital camera. Scanning electron microscopy images were acquired using an FESEM Ultra55 (Zeiss) scanning electron microscope.

Scanning transmission electron microscopy (STEM) coupled with energy-dispersive X-ray spectroscopy (EDS) was used to map Au, Pd, and Si distributions. They were obtained on aberration-corrected TEM, JEOL atomic-resolution analytical TEM—ARM200F at 200 kV.

**2.3. In Situ Characterization Techniques.** Extended X-ray absorption fine structure (EXAFS) technique was used to determine coordination numbers, neighboring atoms, and interatomic distances. X-ray absorption near-edge structure (XANES) studies were used to identify local coordination geometries and metal oxidation states.

The measurements were performed at the SSRL beamline BL 2-2 at the Au L<sub>3</sub>-edge (*E*<sub>0</sub> = 11 919 eV) and Pd K-edge (*E*<sub>0</sub> = 24 350 eV). Measurements for Au L<sub>3</sub>-edge were performed in transmission mode, while for the Pd K-edge, they were performed in fluorescence mode using a 13 channel Ge detector. XAS spectra for Au and Pd foils were collected simultaneously with their respective catalyst spectra and used as references to calibrate and align the acquired spectra in absolute X-ray energy.

The samples were packed into capillaries for in situ experiments. Data for as-prepared samples in helium at room temperature were collected for both samples (Pd<sub>0.02</sub>Au<sub>0.98</sub> and Pd<sub>0.09</sub>Au<sub>0.91</sub>). In situ data were collected for Pd<sub>0.09</sub>Au<sub>0.91</sub> sample only. The sample was heated to 250 °C, and measurements were performed at different partial pressures of oxygen and carbon monoxide (in 2:5 CO and O<sub>2</sub> ratio, 5:2 CO and O<sub>2</sub> ratio, and in pure CO). Afterward, the sample was treated in a H<sub>2</sub> atmosphere (5% H<sub>2</sub> and He mixture, 250 °C), and measurements in 2:5 CO and O<sub>2</sub> atmospheres were repeated. After this treatment cycle, a final measurement was performed at room temperature under a He atmosphere.

The obtained XAS data were aligned, merged, and normalized using ATHENA program.<sup>19</sup> EXAFS data fitting was performed using FEFFIT code.<sup>20</sup> Theoretical photoelectron scattering amplitudes and phase shifts were obtained in self-consistent ab initio calculations with FEFF8.5 code<sup>21</sup> for bulk Pd–Au. The complex exchange–correlation Hedin–Lundqvist potential and default values of muffin-tin radii as provided within the FEFF8.5 code were employed. Amplitude reduction factors *S*<sub>0</sub><sup>2</sup> (0.97 ± 0.03 for Pd and 0.87 ± 0.02 for Au) were obtained from the EXAFS data fits for corresponding foil spectra and later fixed to those values for the determination of coordination numbers in NPs.

Infrared (IR) spectroscopy was performed in a diffuse reflectance infrared Fourier transform spectroscopy (DRIFTS) mode on a Thermo Nicolet iS50 FT-IR spectrometer to study the ν(CO) frequency in the catalytic materials and understand the nature of the active sites at room temperature after exposure to CO.

**2.4. Reactor Study.** Catalytic studies were carried out in a continuous flow reactor at atmospheric pressure. Catalysts were crushed and sieved to obtain particle sizes between 100 and 300 μm. The catalysts were then mixed with quartz sand to minimize hot-spot formation and loaded into a tubular quartz reactor tube (internal diameter: 1 cm). CO oxidation was carried out with a feed gas mixture of CO (5%), O<sub>2</sub> (10%), in a balance of He at atmospheric pressure. The catalysts were tested as-prepared (after calcination in air at 500 °C). Light-off experiments were started at low temperatures on the fresh catalysts. The temperature was then increased step by step, and steady-state conversions were reported. Catalyst performance was evaluated by an online mass spectrometer that was calibrated using He for *m/z* = 4, CO for *m/z* = 28 (with a correction factor taking into account the contribution of CO<sub>2</sub>), O<sub>2</sub> for *m/z* = 32, and CO<sub>2</sub> for *m/z* = 44. Apparent activation energies were derived from the Arrhenius equation considering reaction rates normalized by the amount of Pd at low conversion (10 to 20%) in a differential regime such that the difference between the inlet and outlet concentrations can be directly related to the reaction rate. Stability tests were monitored using a GC/TCD (Agilent Column CarbonPLOT). Internal mass transfer limitations were excluded by the Weisz modulus and verified to be insignificant experimentally by varying the catalyst particle size. External mass transfer limitations were also negligible according to the Carberry number; verification of their insignificance was obtained by varying the volume of the catalytic bed and adjusting the flow rate to keep the gas hourly space velocity constant (Figure S3 and Table S1 in SI).

**2.5. DFT Calculations.** To investigate the surface structures of Pd<sub>x</sub>Au<sub>1-x</sub> alloys, density functional theory (DFT) calculations were performed using the Vienna ab initio simulation package (VASP)<sup>22</sup> with the projector-augmented wave (PAW) potentials.<sup>23,24</sup> The Perdew–Burke–Ernzerhof formulation of the generalized gradient approximation (GGA-PBE)<sup>25</sup> was used for the exchange–correlation functional. The kinetic energy cutoff of the plane-wave basis sets was 400 eV. To include the van der Waals (vdW) interactions, the

Tkatchenko–Scheffler method<sup>26</sup> was used. The lattice constant of bulk Au was obtained to be 4.11 Å, which is close to the experimental value (4.08 Å).

A Au(211)-stepped surface, which includes both terrace and step sites, was modeled to consider the effect of steps, the generally more active sites of a nanoparticle. The surface was modeled by slabs of 12 atomic layers separated by 15 Å of vacuum space. The supercells consisted of  $1 \times 4$  unit cells, resulting in 7.12 and 11.63 Å in the  $x$  and  $y$  directions, respectively. The Pd–Au-alloyed surface was constructed by the selective substitution of Au by Pd in the top 8 layers (32 sites). For CO adsorption, we considered all possible sites on the surface. A  $\gamma$ -centered  $8 \times 5 \times 1$   $k$ -point mesh<sup>27</sup> was utilized. During structural relaxation, the bottom four layers of Au were constrained to the bulk positions, and the remaining atoms were fully relaxed to a force threshold of 0.01 eV/Å.

The DFT total energies of relaxed systems were used to compare the stability of different structures. Due to a large number of possible configurations considered, the zero-point energy and finite temperature effect on the structural stability were ignored. The CO stretch frequencies for the most stable configurations were calculated within the harmonic approximation. The CO adsorbate and the topmost three layers of metal atoms were included in the calculation of the Hessian matrix, whose eigenvalues were the harmonic frequencies.

### 3. RESULTS AND DISCUSSION

**3.1. Synthesis and Characterization of Catalysts Using Standard Methods.** The particles are uniformly distributed in the silica matrix. Before the templating synthesis, the average particle size was  $3.2 \pm 0.8$  nm for self-standing Pd nanoparticles, as determined by TEM. After the templating and calcination, monometallic Pd shows an increase in particle diameter from 3.2 to  $4.8 \pm 1.1$  nm on average (Table 1). For

**Table 1.** Pd<sub>x</sub>Au<sub>1-x</sub> Nanoparticle Size is Preserved After Final Calcination at 500 °C in Air

	self-standing nanoparticles		nanoparticles embedded in RCT-SiO <sub>2</sub> after calcination	
	diameter (nm) <sup>a</sup>		diameter (nm) <sup>a</sup>	atom % Pd <sup>b</sup>
Pd <sub>0.02</sub> Au <sub>0.98</sub>	5.4 ± 1.0		5.8 ± 1.4	2.1 ± 0.4
Pd <sub>0.09</sub> Au <sub>0.91</sub>	5.8 ± 1.2		6.0 ± 2.1	9.5 ± 1.1
Pd	3.2 ± 0.8		4.8 ± 1.1	100

<sup>a</sup>Average particle size as determined by TEM. <sup>b</sup>Measured by ICP-MS.

self-standing Pd<sub>0.02</sub>Au<sub>0.98</sub> and Pd<sub>0.09</sub>Au<sub>0.91</sub> nanoparticles, the average particle sizes were  $5.4 \pm 1.0$  and  $5.8 \pm 1.2$  nm, respectively (Table 1). The average particle size of bimetallic materials was preserved after calcination within the error bars. The resulting catalytic material is a highly structured silica matrix presenting voids of around 380 nm interconnected by 80 nm windows (Figure 1d). The particles are embedded in the silica support (Figure 1e). In contrast, pure Au nanoparticles impregnated on preformed RCT-SiO<sub>2</sub> structures rapidly sinter upon calcination, leading to an increase in the nanoparticle diameter from  $4.2 \pm 0.4$  to  $19.3 \pm 5.8$  nm (Figure S7). Together, these results demonstrate that the partial embedding of the nanoparticles in the silica imparts a high degree of thermal stability to the catalyst structure. The average composition of the nanoparticles was measured using ICP-MS (Table 1) and was very close to the nominal composition. The total surface area of the RCT-SiO<sub>2</sub> without nanoparticles was measured to be 210 m<sup>2</sup> g<sup>-1</sup> by BET. The metal surface area for the Pd–Au RCT-SiO<sub>2</sub> was estimated using TEM images to be 100 m<sup>2</sup> g<sup>-1</sup>, assuming a 5% embedding of the particle in the silica matrix.

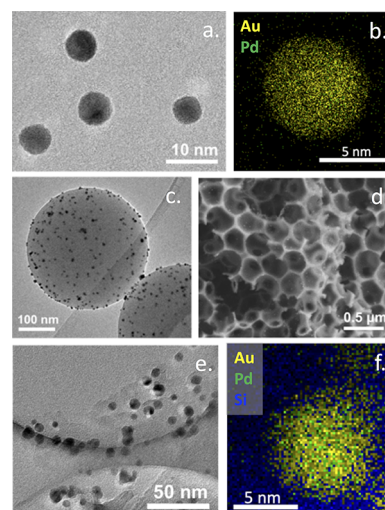


**Figure 1.** Nanoparticles are synthesized and then embedded in silica using the colloid-templated approach to form the catalytic material as shown by (a) TEM and (b) STEM–EDS map of self-standing Pd<sub>0.09</sub>Au<sub>0.91</sub> particles (see Methods); (c) TEM image of the raspberry colloid Pd@Pd<sub>0.09</sub>Au<sub>0.91</sub> showing the NPs decorating the modified polystyrene beads; (d) SEM of the catalyst after the assembly of raspberry colloids, infiltration of the silica precursor, and calcination to remove the polystyrene; (e) TEM; and (f) STEM–EDS map of Pd<sub>0.09</sub>Au<sub>0.91</sub> RCT-SiO<sub>2</sub>.

Pd appeared uniformly distributed in Au in both the self-standing particles (Figure 1a,b) and after the templating synthesis (Figure 1f). Neither Pd nor Au appears to migrate onto the silica (Figure 1f).

**3.2. Catalyst Performance.** Full CO conversion was achieved at different temperatures over the different as-prepared bimetallic catalysts; the lower the Pd concentration, the higher was the temperature (Figure 2). Silica alone,

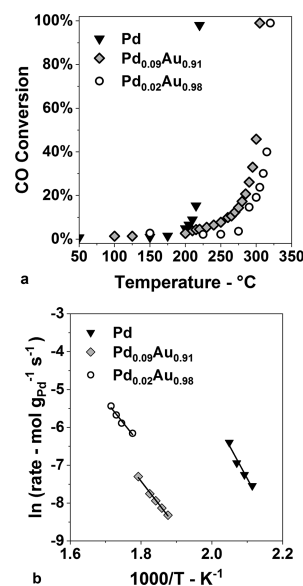


**Figure 2.** (a) CO conversion vs temperature to activate the catalysts of different Pd compositions. These light-off curves depend on the Pd concentration. (b) Apparent activation energies for Pd and the two Pd<sub>x</sub>Au<sub>1-x</sub> bimetallics are similar; reaction conditions: 5% CO, 10% O<sub>2</sub> in He balance; GHSV = 2000 h<sup>-1</sup>; total flow rate = 25 mL min<sup>-1</sup>;  $m(\text{Pd}_{0.09}\text{Au}_{0.91}, \text{Pd}_{0.02}\text{Au}_{0.98}) = 40$  mg;  $m(\text{Pd}) = 10$  mg.



without nanoparticles, was not active for CO oxidation over the range of temperature studied (Figure S2). Pure Pd was more active at a lower temperature than Pd<sub>0.09</sub>Au<sub>0.91</sub> RCT-SiO<sub>2</sub> with full conversions achieved at 215 and 300 °C, respectively. Pd<sub>0.02</sub>Au<sub>0.98</sub> showed full conversion at the highest temperature ( $T_{100\%} = 320$  °C).

The apparent activation energies for CO oxidation in the light-off of the three catalysts are  $119 \pm 5$  kJ mol<sup>-1</sup> over Pd,  $92 \pm 8$  kJ mol<sup>-1</sup> over Pd<sub>0.09</sub>Au<sub>0.91</sub>, and  $112 \pm 15$  kJ mol<sup>-1</sup> over Pd<sub>0.02</sub>Au<sub>0.98</sub> and showed no discernible dependence on the Pd content (Figure 2b). They compare well with activation energies of CO oxidation measured on model silica-supported Pd catalysts over the same range of temperature (104.5–113 kJ mol<sup>-1</sup>).<sup>28</sup> Extensive studies of single crystals Pd(100), Pd(111), and Pd(110) elucidated that activation energies of CO oxidation are actually CO desorption energies (104.5–121 kJ mol<sup>-1</sup> at 0.5 CO coverage).<sup>29–31</sup> Indeed, the Langmuir–Hinshelwood reaction between adsorbed O and adsorbed CO is a well-established mechanism for CO oxidation over Pd, where CO and O<sub>2</sub> compete for active sites. At low temperature and rate, the surface is covered with CO and the reaction rate is controlled by its desorption.<sup>32</sup> At higher temperatures, the CO desorption rate and the oxygen adsorption rate increase and thus the oxidation rate increases.

On the other hand, the CO desorption energy on Au is much lower ( $10 < E_d < 40$  kJ mol<sup>-1</sup> on Au(110),<sup>33,34</sup>  $27 < E_d < 50$  kJ mol<sup>-1</sup> on Au(211),<sup>35</sup> and 55–58 kJ mol<sup>-1</sup> at low coverages on Au(100)<sup>36</sup> and Au(332)<sup>37</sup>). Very few CO oxidation activation energies over Au–SiO<sub>2</sub> catalysts have been reported in the literature, but studies with different metal oxide supports fall within the same range (16.3–50 kJ mol<sup>-1</sup>).<sup>8,38</sup> Based on the fact that the apparent activation energies observed over the Pd<sub>x</sub>Au<sub>1-x</sub> catalysts are close to those observed for pure Pd catalysts, the reaction on Pd sites appears to drive the kinetics for the oxidation of CO on the unconditioned as-prepared catalyst. Surface Pd species thus play a critical role in the CO oxidation over the Pd<sub>0.02</sub>Au<sub>0.98</sub> and Pd<sub>0.09</sub>Au<sub>0.91</sub> RCT-SiO<sub>2</sub>.

The measured activation energies may, however, not be so simply interpretable. Hysteresis was observed as the temperature was decreased after a light-off experiment over Pd<sub>0.02</sub>Au<sub>0.98</sub> RCT-SiO<sub>2</sub>: the activity was enhanced at low temperature (Figure 3). It is thus possible that the light-off experiments induce substantial modifications that could be

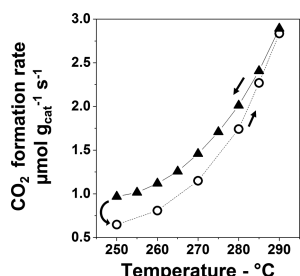


**Figure 3.** Rates of CO oxidation are significantly enhanced at low temperature after the light-off experiment over Pd<sub>0.02</sub>Au<sub>0.98</sub> RCT-SiO<sub>2</sub>. Steady-state rates are reported as the temperature is (○) increased during the light-off experiment, (▲) decreased after the light-off experiment. The arrow at low temperature indicates that the process is reversible after calcination at 500 °C; reaction conditions: 5% CO, 10% O<sub>2</sub> in He balance; GHSV = 2000 h<sup>-1</sup>; total flow rate = 25 mL min<sup>-1</sup>;  $m(\text{Pd}_{0.02}\text{Au}_{0.98}) = 40$  mg.

attributed to a change in oxidation states and/or a redistribution of Pd in Au when the catalyst is exposed to the reactant mixtures over this wide range of temperature. A more detailed mechanistic study is underway to investigate how conditioning, i.e., pretreatment, influences the state of the catalyst and the reaction rate by evaluating apparent activation energies and reaction orders of CO and O<sub>2</sub> over a wide range of temperatures and pressures.

**3.3. Stability of Pd<sub>0.09</sub>Au<sub>0.91</sub> RCT-SiO<sub>2</sub>.** No deactivation of the Pd<sub>0.09</sub>Au<sub>0.91</sub> RCT-SiO<sub>2</sub> catalyst was observed at 250 °C under reaction conditions for more than 20 h on stream (Figure 3). The sequential reaction carried out at 280 °C over the same catalytic bed after in situ calcination at 500 °C confirms that the catalyst is highly stable. TEM images indicated that the average particle size remained unchanged after reaction ( $5.6 \pm 1.3$  nm) within the experimental error from that measured for the as-prepared sample ( $6.3 \pm 1.3$  nm) (Figure 4). The highly ordered silica structure was also

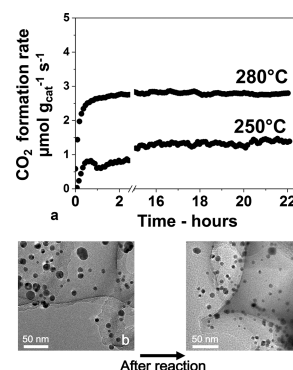


**Figure 4.** (a) Pd<sub>0.09</sub>Au<sub>0.91</sub> RCT-SiO<sub>2</sub> is stable for CO oxidation over time-on-stream at high temperatures. The nanoparticles do not appear to sinter after reaction, as evidenced by TEM images of Pd<sub>0.09</sub>Au<sub>0.91</sub> (b) before reaction and (c) after more than 40 h of reaction; reaction conditions:  $T = 250$  and  $280$  °C; 5% CO, 10% O<sub>2</sub> in He balance; GHSV = 2000 h<sup>-1</sup>; total flow rate = 25 mL min<sup>-1</sup>;  $m = 40$  mg.

preserved. The Pd<sub>x</sub>Au<sub>1-x</sub> RCT-SiO<sub>2</sub> catalysts are thus very stable at high temperature under reaction conditions. This property is critically different from typical gold catalysts, as Au and Au–Pd nanoparticles are very much prone to sintering during calcination and reaction<sup>6,39</sup> and, in general, prone to deactivation.<sup>8,9</sup> The templating synthesis approach prevents sintering at high temperature by stabilizing the embedded nanoparticles in the silica matrix.

These experiments indicate that Pd is likely to play a major role in the activity of the bimetallic catalysts. Therefore, extensive studies were undertaken to understand the distribution of Pd between the bulk and surface as a function of the initial bulk concentration under both as-prepared and reaction conditions.

**3.4. EXAFS and XANES Over As-Prepared Pd<sub>0.02</sub>Au<sub>0.98</sub> and Pd<sub>0.09</sub>Au<sub>0.91</sub> RCT-SiO<sub>2</sub> at Room Temperature.** The oxidation state and structural parameters of Au in as-prepared Pd<sub>0.02</sub>Au<sub>0.98</sub> and Pd<sub>0.09</sub>Au<sub>0.91</sub> are very similar to that in bulk fcc Au according to XANES and EXAFS measurements (Figure 5a,c). The amplitudes of the main peaks (corresponding to the contribution of the first nearest-neighboring pairs) in Fourier-transformed (FT) Au L<sub>3</sub>-edge EXAFS spectra are slightly lower for the Pd–Au catalysts than for the foil due to either the

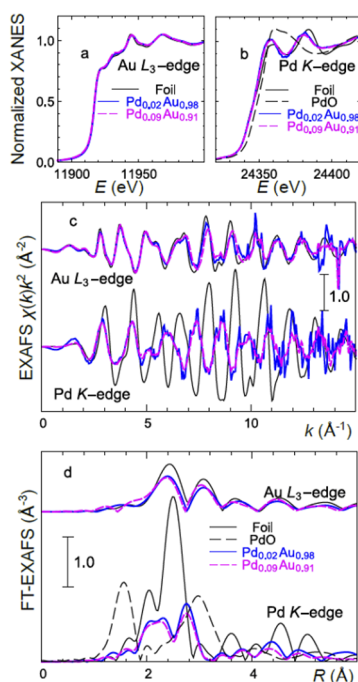


**Figure 5.** XANES spectra for the as-prepared catalyst showing the Au L<sub>3</sub>-edge (a) and Pd K-edge (b) in Pd<sub>0.09</sub>Au<sub>0.91</sub> and Pd<sub>0.02</sub>Au<sub>0.98</sub> samples. Corresponding k<sup>2</sup>-weighted EXAFS spectra and magnitudes of Fourier-transformed EXAFS spectra are shown in (c) and (d). Spectra for Au foil, Pd foil, and PdO are shown for comparison.<sup>40</sup> Spectra in (c) and (d) are shifted vertically for clarity. Au spectra are typical of bulk gold, and Pd is metallic and well distributed in the Au.

particle size effect or enhanced bond length disorder in Au environment or both (Figure 5d).

Pd is predominantly metallic and surrounded by Au atoms in both Pd<sub>0.02</sub>Au<sub>0.98</sub> and Pd<sub>0.09</sub>Au<sub>0.91</sub> RCT-SiO<sub>2</sub>. Shapes and positions of the main features in XANES spectra for Pd K-edge are resembling those in the spectrum for Pd foil and are very different from the effects (the height and energy of the absorption peak maximum) observed in oxidized Pd compounds (Figure 5b).<sup>40,41</sup> This conclusion is also supported by the EXAFS data: the presence of low-Z elements, which would be attributed to the presence of O in the first shell, is not observed (Figure 5c,d). Instead, the data is consistent with the presence of Au in the first shell, not just Pd as in the foil.

For the fresh samples, the values of structural parameters obtained from quantitative fitting of the EXAFS are in excellent agreement with those inferred from the independently determined nanoparticle size (TEM) and composition (ICP-MS) (Table 2 and Figure S3 in SI). First, the coordination

number for Au–Pd bond in Pd<sub>0.09</sub>Au<sub>0.91</sub> NPs is larger than in Pd<sub>0.02</sub>Au<sub>0.98</sub>, which can be linked to the difference in Pd concentration in these samples. Since the total number of Pd–Au bonds is the same as the number of Au–Pd bonds, the ratio of Pd–Au and Au–Pd coordination numbers should be equal to the ratio of Au and Pd atoms  $n_{\text{Au}}/n_{\text{Pd}}$ ,<sup>42</sup> provided, as appears to be the case, that there are no Pd–Pd clusters. In the case of Pd<sub>0.09</sub>Au<sub>0.91</sub> NPs, the ratio of Pd–Au and Au–Pd coordination numbers is close to 10, which corresponds to a Pd concentration of approximately 9%, while for Pd<sub>0.02</sub>Au<sub>0.98</sub> NPs, this ratio is approximately 40, which corresponds to a Pd concentration of 2%.

The average metal–metal coordination number can be calculated from EXAFS coordination numbers as

$$N_{\text{metal}} = \frac{n_{\text{Pd}}N_{\text{Pd}} + n_{\text{Au}}N_{\text{Au}}}{n_{\text{Pd}} + n_{\text{Au}}} = \frac{N_{\text{Pd}} + (n_{\text{Au}}/n_{\text{Pd}})N_{\text{Au}}}{1 + n_{\text{Au}}/n_{\text{Pd}}}$$

where  $N_{\text{Pd}}$  is the total Pd coordination number ( $N_{\text{Pd-Pd}} + N_{\text{Pd-Au}}$ ) and  $N_{\text{Au}}$  is the total Au coordination number ( $N_{\text{Au-Pd}} + N_{\text{Au-Au}}$ ).<sup>42</sup> From this equation, we obtain that  $N_{\text{metal}}$  is  $11.3 \pm 0.6$  for Pd<sub>0.09</sub>Au<sub>0.91</sub>, which corresponds to particles with a size of 5–6 nm,<sup>43,44</sup> in excellent agreement with TEM results. The same calculations are not conclusive for the Pd<sub>0.02</sub>Au<sub>0.98</sub> sample due to larger uncertainties in coordination numbers.

In these catalysts, Pd atoms appear to be completely dispersed within the gold, and no agglomeration of Pd is detectable as indicated by the lack of Pd–Pd bonds ( $N_{\text{Pd-Pd}}$  in Table 2). The alloying of Au and Pd is confirmed by the analysis of interatomic distances: the Au–Au distance in the NP samples is smaller than in bulk gold and decreases with increasing Pd concentration, in agreement with Vegard's law characterizing random alloy behavior.

The majority of Pd atoms are fully coordinated and are not exposed to the particle surface, which consists mostly of gold atoms.<sup>4</sup> Indeed, the total Pd coordination number is close to 12 and is slightly larger than the total Au coordination number for both catalysts. The presence of a small fraction of Pd atoms on the particle surface, however, cannot be ruled out due to the significant error bar for Pd coordination numbers. Calculations showed that if less than 30% of Pd would segregate to the surface, the first shell coordination number would not be significantly affected (Section S4 in SI).

The disorder is characterized here by the factor  $\sigma^2$ , also called Debye–Waller factor, which describes the variance in the bond length. Such disorder can be attributed to structural and/or thermal changes and is larger in NPs than in bulk materials.<sup>45</sup> It is also typical for nanosized alloys and is evidence of alloying-induced or surface-induced strain. The disorder effects are more pronounced for Pd<sub>0.02</sub>Au<sub>0.98</sub> than for

**Table 2. Structure Parameters (Coordination Numbers  $N$ , Interatomic Distances  $R$ , and Disorder Factors  $\sigma^2$ ) Obtained in Fitting of Experimental EXAFS Data for Fresh Pd<sub>0.02</sub>Au<sub>0.98</sub> and Pd<sub>0.09</sub>Au<sub>0.91</sub> Samples<sup>a</sup>**

sample	$N_{\text{Au-Au}}$	$R_{\text{Au-Au}}$ (Å)	$\sigma_{\text{Au-Au}}^2$ (Å <sup>2</sup> )	$N_{\text{Au-Pd}}$	$R_{\text{Au-Pd}}$ (Å)	$\sigma_{\text{Au-Pd}}^2$ (Å <sup>2</sup> )	$\Delta E_0$ (Au) (eV)	R factor (%)
Au foil	12	2.859(2)	0.0084(3)				5.3(2)	1.0
Pd <sub>0.09</sub> Au <sub>0.91</sub> , fresh	10.0(6)	2.832(3)	0.0098(7)	1.2(2)	2.811(6)	0.0094(8)	4.8(3)	3.1
Pd <sub>0.02</sub> Au <sub>0.98</sub> , fresh	11(1)	2.856(5)	0.011(1)	0.3(3)	2.82(1)	0.009(2)	5.6(6)	2.1
sample	$N_{\text{Pd-Au}}$	$R_{\text{Pd-Au}}$ (Å)	$\sigma_{\text{Pd-Au}}^2$ (Å <sup>2</sup> )	$N_{\text{Pd-Pd}}$	$R_{\text{Pd-Pd}}$ (Å)	$\sigma_{\text{Pd-Pd}}^2$ (Å <sup>2</sup> )	$\Delta E_0$ (Pd) (eV)	R factor (%)
Pd foil				12	2.741(1)	0.0059(2)	−4.5(2)	0.6
Pd <sub>0.09</sub> Au <sub>0.91</sub> , fresh	12.0(9)	2.811(6)	0.0094(8)	0			−6.1(5)	1.7
Pd <sub>0.02</sub> Au <sub>0.98</sub> , fresh	12(3)	2.82(1)	0.009(2)	0			−5(2)	1.4

<sup>a</sup>Uncertainties in the last significant digits are shown in parentheses.

$\text{Pd}_{0.09}\text{Au}_{0.91}$ . Together with the observed differences in interatomic distances, the structure strain can be a reason for differences in catalytic properties of the investigated nanocatalysts.<sup>46,47</sup>

Conventional EXAFS analysis presents a useful cross-check with TEM and ICP results (Table 2) but the key detail about the local composition motifs (are the elements homogeneously mixed, and, if not, what type of heterogeneity they embed) is missing. These limitations are due to the fact that conventional EXAFS data analysis relies predominantly on the parameters of the first coordination shell. The large error bars in the best-fit results and too crude a model did not conclusively answer the question about the minority atom (Pd) location within the majority atom (Au) host (Table 2). Indeed, only Pd–Au was allowed to contribute to the data in the case of Pd edge because adding the contribution of Pd–Pd, expected to be very minor, made the fit unstable.

On the other hand, a recently developed method based on the artificial neural network and molecular dynamics simulations allowed us to extract such information from the higher-order shells, using a partial radial distribution function (PRDF) analysis approach.<sup>48</sup> Using the same spectra for the 2 and 9% Pd samples as in the present work, we showed that the Pd–Au distances corresponding to the second nearest-neighbor shell in the fcc structure were distinctly lower than those corresponding to the random alloy behavior.<sup>48</sup> That observation is consistent with Pd atoms having a tendency to segregate toward the surface of Au–Pd nanoparticles (where the interatomic distances are expected to be shortened by surface-induced tensile stress). In addition, the total Pd coordination numbers for all distant coordination shells were found to be lower than the corresponding total coordination numbers for Au, suggesting the presence of undercoordinated Pd sites. Note that the sample with the lowest Pd concentration provides the best sensitivity to observe such a trend.

**3.5. In Situ EXAFS and XANES Over  $\text{Pd}_{0.09}\text{Au}_{0.91}$  RCT-SiO<sub>2</sub> Under CO Oxidation Reaction.** Oxidation states of Au and Pd atoms do not change significantly during CO oxidation reaction, as determined with in situ XAS data for  $\text{Pd}_{0.09}\text{Au}_{0.91}$  RCT-SiO<sub>2</sub> sample, collected at 250 °C and different CO and O<sub>2</sub> partial pressures (Figure 6). In all cases, XANES spectra, collected at Au L<sub>3</sub>-edge (Figure 6a) and Pd K-edge (Figure 6b), are very similar to those for the fresh sample.

The structure of  $\text{Pd}_{0.09}\text{Au}_{0.91}$  does not change significantly since changes in Pd K-edge EXAFS spectra are also minor (Figure 6c,d). Only a small reduction of the amplitude of EXAFS features was detected, which can be attributed to an increase in thermal disorder. After cooling the sample back to room temperature, its EXAFS spectrum becomes very similar to that in the fresh sample. Slightly larger amplitudes of the main FT-EXAFS features for the sample after the treatment cycle can be explained by a reduction of static disorder in the annealing-like process.

During CO oxidation, no change in coordination numbers in  $\text{Pd}_{0.09}\text{Au}_{0.91}$  could be detected within error bars of our analysis. The results of fitting of the in situ Pd K-edge data for  $\text{Pd}_{0.09}\text{Au}_{0.91}$  RCT-SiO<sub>2</sub> during CO oxidation show no change in coordination numbers compared to the as-prepared measurements within error bars of the analysis (Figure S4 and Table S2 in SI). The observed differences in EXAFS spectra can be fully explained by an increase of thermal disorder (Debye–Waller factors). At the same time, a minor

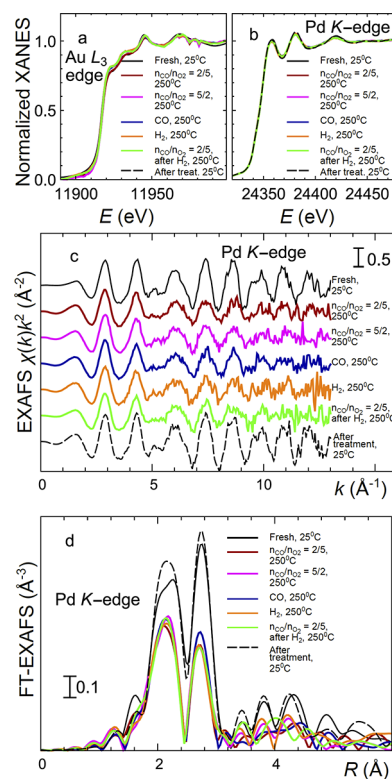


**Figure 6.** In situ XANES spectra under reaction conditions for Au L<sub>3</sub>-edge (a) and Pd K-edge (b) in  $\text{Pd}_{0.09}\text{Au}_{0.91}$  samples. Corresponding EXAFS spectra and magnitudes of Fourier-transformed,  $k^2$ -weighted, EXAFS spectra are shown in (c) and (d). Spectra in (c) are shifted vertically for clarity. No differences from the as-prepared catalyst were detected.

shortening of Pd–Au distance can be detected during the sample treatment, and slightly shorter Pd–Au distance and slightly smaller disorder factor were obtained for the sample at room temperature after treatment, which can be interpreted as an evidence of some structure relaxation during the sample heating and cooling cycles.

In summary, according to EXAFS and XANES, Au and Pd are metallic in  $\text{Pd}_x\text{Au}_{1-x}$  RCT-SiO<sub>2</sub> catalysts. Pd is atomically distributed within the gold host particles; the presence of some fraction of Pd atoms on the NP surface cannot be excluded. These appear to hold for both the fresh catalyst and the working catalyst during CO oxidation. Whether Pd exists at the surface of the nanoparticles, where the catalytic reaction occurs, could not be discerned by XAS analysis. Further investigation of the distribution of Pd on the surface was thus undertaken using diffuse reflectance infrared Fourier transform spectroscopy (DRIFTS).

**3.6. Surface Investigation with CO-DRIFTS.** Based on the measured  $\nu(\text{CO})$  frequency observed for the Au,  $\text{Pd}_{0.02}\text{Au}_{0.98}$ ,  $\text{Pd}_{0.09}\text{Au}_{0.91}$ , and Pd RCT-SiO<sub>2</sub> catalysts after exposure to CO (Figure 7), Pd appears to be present on the surface of the alloy catalysts, its distribution depending on the Pd concentration in the particles (Figure 7 and Table 3). Infrared (IR) spectra of the carbonyl region on monometallic Pd show predominant bands at 1989 cm<sup>-1</sup> that can be attributed to bridged-bonded CO on Pd. It also shows bands at 2092 assignable to atop CO on Pd sites.<sup>30,49</sup>

Monometallic Au shows atop CO on Au sites at 2132 cm<sup>-1</sup>.<sup>50</sup>  $\text{Pd}_{0.09}\text{Au}_{0.91}$  shows three different adsorption bands:



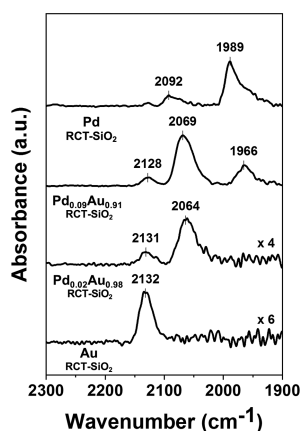


**Figure 7.** Pd is present at the surface of Pd<sub>0.02</sub>Au<sub>0.98</sub> and Pd<sub>0.09</sub>Au<sub>0.91</sub> as observed by CO-DRIFTS spectra of Au, Pd<sub>0.02</sub>Au<sub>0.98</sub>, Pd<sub>0.09</sub>Au<sub>0.91</sub>, and Pd RCT-SiO<sub>2</sub> after reduction at 250 °C for 1 h and exposure to CO for 20 min at room temperature. Pd appears to be atomically dispersed at the surface for the 2% catalyst.

2128, 2069, and 1966 cm<sup>-1</sup> that can be assigned to CO atop Au, CO atop Pd, and bridged CO, respectively.<sup>51</sup> Pd<sub>0.02</sub>Au<sub>0.98</sub>, in turn, only showed two adsorption bands at 2131 and 2064 cm<sup>-1</sup> assigned to atop CO on Au and atop CO on isolated Pd in Au.

From these results, it is possible to conclude that Pd is atomically distributed in Pd<sub>0.02</sub>Au<sub>0.98</sub> after exposure to CO at room temperature. Both isolated and clustered Pd appear to be present in Pd<sub>0.09</sub>Au<sub>0.91</sub>.

**3.7. CO Adsorption and Stretch Frequency Calculations with DFT.** CO adsorption structures were calculated on the Au(211)- and the Pd–Au(211)-alloyed surfaces. It has been a standing puzzle<sup>52</sup> that DFT predicts wrong site preference for CO adsorption on several metal surfaces including Au. Here, calculations show that CO adsorption at the atop and at the bridge sites of the Au(211) step edge are the two lowest-energy structures. They have almost degenerate energies (differed by 0.01 eV, Table 4), in contradiction to the preference of atop site observed experimentally.<sup>35</sup>

The two lowest-energy structures for CO adsorption on Pd–Au have Pd positioned at the topmost layer (Table 4, CO/Pd–Au). This implies that the strong interaction between CO and Pd stabilizes Pd on the surface. Bridge bonding between CO with one Pd and one Au at the step edge is less stable than with the atop site of Pd by 0.13 eV. As more Pd is added, the added Pd prefers to stay at the fourth layer; one CO molecule seems to stabilize only one Pd on the surface.

The CO stretch frequencies computed with DFT compare generally well with conclusions based on the experiment. CO adsorbed at the bridge sites exhibits much smaller stretch

frequencies than at the atop sites (Table 4). The experimental frequencies (DRIFTS) suggest that CO is adsorbed at the atop sites on both Au(211) and Pd–Au(211) surfaces. However, there are quantitative differences between the DFT and experimental frequencies. These differences are, in part, due to the systematic error within DFT, as seen in the overestimated gas-phase CO frequency (Table 4). The variation of CO concentration and surface structures under reaction conditions can also lead to discrepancies between theoretical and experimental results. However, the qualitative trend of the lower CO frequency on Pd-doped Au compared to that on the Au surface is consistent with our experimental results.

EXAFS results taken under helium at room temperature and under reaction conditions at 250 °C indicated that Pd in the Pd<sub>x</sub>Au<sub>1-x</sub> catalysts is predominantly atomically distributed in the bulk of the host Au. In addition, CO-DRIFTS revealed that atomically distributed Pd exists at the surface after exposure to CO at room temperature. For the higher Pd concentrations (Pd<sub>0.09</sub>Au<sub>0.91</sub>), clusters of Pd atoms may also exist at the surface. According to our EXAFS study, the Pd clusters on Pd<sub>0.09</sub>Au<sub>0.91</sub> must represent less than 30% of the total Pd (calculations in SI). It must be emphasized that the CO-DRIFTS measurements were taken at room temperature after exposure to CO for 20 min. Recent studies on Pd–Au and Pd–Ag bimetallic catalysts and surfaces strongly suggest that CO environment can induce the segregation of Pd to the surface.<sup>53,54</sup> The DFT calculations further indicate this possibility.

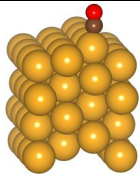
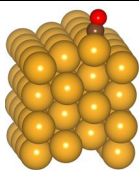
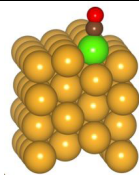
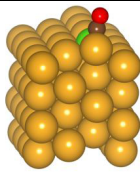
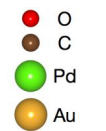
Restructuring of supported Pd–Au bimetallic catalyst with a nominal Pd/Au ratio of 1:1 has been reported using combined XAFS-DRIFTS. The starting material, inferred to be a Au core with surface Pd–Au alloy and surface PdO islands, was shown to undergo reduction and Pd segregation to the surface during CO oxidation at 240 °C, resulting in a core–shell structure (Pd shell, Au core).<sup>55</sup> The lack of evidence of Pd segregation observed here at similar temperatures for the Pd<sub>x</sub>Au<sub>1-x</sub> RCT-SiO<sub>2</sub> could be attributed to the much more dilute Pd concentration. Under ultrahigh vacuum conditions, strong Au segregation to the surface was evidenced for all bulk Pd–Au ratios, which is generally understood to be caused by the fact that Au has smaller free energy than Pd.<sup>56</sup> The dilute alloys thus provide a surface low in Pd that affords catalytic behavior that differs from the catalysts of higher Pd content. In situ characterization techniques are thus crucial to the understanding of active sites of these alloy catalysts during the reaction. Complementary studies are underway to determine how the Pd distribution in Pd<sub>x</sub>Au<sub>1-x</sub> RCT-SiO<sub>2</sub> bimetallic systems can be further tuned by pretreatments and reaction conditions to create different pathways for oxidation reactions.

**Table 3.** CO Adsorption Bands Over Au, Pd, Pd<sub>0.09</sub>Au<sub>0.91</sub>, and Pd<sub>0.02</sub>Au<sub>0.98</sub> RCT-SiO<sub>2</sub> and Their Assignments

	CO/Au atop cm <sup>-1</sup>	CO/Pd atop cm <sup>-1</sup>	CO/Pd bridge cm <sup>-1</sup>	references
Pd RCT-SiO <sub>2</sub>		2092	1989	this work
Au RCT-SiO <sub>2</sub>	2132			this work
Pd <sub>0.09</sub> Au <sub>0.91</sub> RCT-SiO <sub>2</sub>	2118	2069	1966	this work
Pd <sub>0.02</sub> Au <sub>0.98</sub> RCT-SiO <sub>2</sub>	2131	2064		this work
Pd(111) surface		2110–2080	1965–1900 <sup>a</sup> ; 1900–1800 <sup>b</sup>	30, 49
Pd–Au surface	2105	2087	1940	51

<sup>a</sup>2-fold-bridged CO. <sup>b</sup>3-fold-bridged CO.

**Table 4. Relative Energies, Carbon–Metal Distances, DFT, and Experimental Stretch Frequencies of CO Adsorbed at the Atop and Bridge Sites of Au and Pd–Au Surfaces<sup>a</sup>**

	CO( <i>g</i> )	CO/Au		CO/PdAu	
Adsorption site	–	atop	bridge	atop	bridge
Structure	–				
					
Relative E (eV)	–	0.00	–0.01	0.00	+0.13
$d_{\text{C-metal}}$ (Å)	–	1.97	2.12	1.89	1.95
DFT $\nu_{\text{CO}}$ (cm <sup>-1</sup> )	2123.6	2055.7	1884.8	2031.7	1914.6
Exp $\nu_{\text{CO}}$ (cm <sup>-1</sup> )	2143 <sup>35</sup>	2112–2126 <sup>35</sup>	–	~2070	–

<sup>a</sup>The frequencies for gas-phase CO is also included for the purpose of comparison. The energies of atop-site adsorption structures are set at zero.  $d_{\text{C-metal}}$  measures the distance from C to the closest metal.

#### 4. CONCLUSIONS

Pd<sub>x</sub>Au<sub>1-x</sub> embedded in colloid-templated silica are highly homogeneous bimetallic catalysts. The nanoparticles are stabilized with respect to sintering by embedding in the silica support and remain stable after calcination in air at high temperature. Most importantly, the catalysts, despite their low Pd concentrations, activate O<sub>2</sub> and readily catalyze CO oxidation. The nanoparticles do not appear to sinter at high temperature under reaction conditions and over a long time-on-stream.

Pd plays a crucial role in the activity of the catalyst, and its distribution and oxidation state were thoroughly studied: on the calcined catalyst, Pd and Au are predominantly alloyed in both the Pd<sub>0.09</sub>Au<sub>0.91</sub> and Pd<sub>0.02</sub>Au<sub>0.98</sub> RCT-SiO<sub>2</sub>. Pd is stabilized in its metallic state. In situ XAS analysis indicates that this holds true under CO oxidation reaction conditions at 250 °C. At room temperature and after exposure to CO, Pd is preferably atomically distributed in Au at low concentration (~2 atom %). In turn, for higher concentrations (9 atom %), both Pd atoms and clusters are present on the surface. Complementary theoretical calculations indicate that CO stabilizes Pd at the surface.

Additional work is needed to further understand how Pd surface distribution influences the catalytic performances. Overall, Pd<sub>x</sub>Au<sub>1-x</sub> RCT-SiO<sub>2</sub> are resistant Au-based catalytic materials that open a wide range of possibility for selective oxidation reactions at low and high temperatures.

#### ■ ASSOCIATED CONTENT

##### 📄 Supporting Information

The Supporting Information is available free of charge on the ACS Publications website at DOI: [10.1021/acs.chemmater.9b01779](https://doi.org/10.1021/acs.chemmater.9b01779).

The supporting information contains details about the synthesis of the materials, control experiments, estimations of mass transfer limitations, results of quantitative

fits of experimental EXAFS, and calculations regarding the reliability of detection with XAS (PDF)

#### ■ AUTHOR INFORMATION

##### Corresponding Author

\*E-mail: [rmadix@seas.harvard.edu](mailto:rmadix@seas.harvard.edu).

##### ORCID

Wei Chen: 0000-0003-3598-2369

Anatoly I. Frenkel: 0000-0002-5451-1207

Cynthia M. Friend: 0000-0002-8673-9046

Robert J. Madix: 0000-0002-3132-2382

##### Author Contributions

C.M.F., J.A., A.I.F., and R.J.M. guided the research; E.K. and M.F.-S. participated in discussions; M.L., J.T., and W.C. co-wrote the paper; T.S. designed and conducted the preparation of the materials; M.L. and A.F. designed the flow reactor study; J.T. and M.L. designed the XAS study; A.T. and M.L. designed the CO-DRIFTS study; and W.C. performed the theoretical calculations.

##### Notes

The authors declare no competing financial interest.

#### ■ ACKNOWLEDGMENTS

This work was supported as part of the Integrated Mesoscale Architectures for Sustainable Catalysis (IMASC), an Energy Frontier Research Center funded by the U.S. Department of Energy, Office of Science, Basic Energy Sciences under Award #DE-SC0012573. The authors thank Dr Michael Aizenberg for helpful discussions.

#### ■ REFERENCES

(1) Cao, E.; Sankar, M.; Firth, S.; Lam, K. F.; Bethell, D.; Knight, D. K.; Hutchings, G. J.; McMillan, P. F.; Gavrilidis, A. Reaction and Raman Spectroscopic Studies of Alcohol Oxidation on Gold–



palladium Catalysts in Microstructured Reactors. *Chem. Eng. J.* **2011**, *167*, 734–743.

(2) Liu, J.; Shan, J.; Lucci, F. R.; Cao, S.; Sykes, E. C. H.; Flytzanistephanopoulos, M. Palladium-Gold Single Atom Alloy Catalysts for Liquid Phase Selective Hydrogenation of 1-Hexyne. *Catal. Sci. Technol.* **2017**, *7*, 4276–4284.

(3) Hutchings, G. J. Methane Activation by Selective Oxidation. *Top. Catal.* **2016**, *59*, 658–662.

(4) Hutchings, G. J. Nanocrystalline Gold and Gold Palladium Alloy Catalysts for Chemical Synthesis. *Chem. Commun.* **2008**, 1148–1164.

(5) Whiting, G. T.; Kondrat, S. A.; Hammond, C.; Dimitratos, N.; He, Q.; Morgan, D. J.; Dummer, N. F.; Bartley, J. K.; Kiely, C. J.; Taylor, S. H.; et al. Methyl Formate Formation from Methanol Oxidation Using Supported Gold – Palladium Nanoparticles. *ACS Catal.* **2015**, *5*, 637–644.

(6) Olmos, C. M.; Chinchilla, L. E.; Delgado, J. J.; Hungria, A. B.; Blanco, G.; Calvino, J. J.; Chen, X. CO Oxidation over Bimetallic Au-Pd Supported on Ceria-Zirconia Catalysts: Effects of Oxidation Temperature and Au:Pd Molar Ratio. *Catal. Lett.* **2016**, *146*, 144–156.

(7) Venezia, A. M.; Liotta, L. F.; Pantaleo, G.; La Parola, V.; Deganello, G.; Beck, A.; Koppány, Z.; Frey, K.; Horvath, D.; Guzzi, L. Activity of SiO<sub>2</sub> Supported Gold-Palladium Catalysts in CO Oxidation. *Appl. Catal., A* **2003**, *251*, 359–368.

(8) Xu, J.; White, T.; Li, P.; He, C.; Yu, J.; Yuan, W.; Han, Y. Biphasic Pd-Au Alloy Catalyst for Low-Temperature CO Oxidation. *J. Am. Chem. Soc.* **2010**, *132*, 10398–10406.

(9) Scott, R. W. J.; Sivadinarayana, C.; Wilson, O. M.; Yan, Z.; Goodman, D. W.; Crooks, R. M. Titania-Supported PdAu Bimetallic Catalysts Prepared from Dendrimer-Encapsulated Nanoparticle Precursors. *J. Am. Chem. Soc.* **2005**, *127*, 1380–1381.

(10) Samanta, A.; Rajesh, T.; Devi, R. N. Confined Space Synthesis of Fully Alloyed and Sinter-Resistant AuPd Nanoparticles Encapsulated in Porous Silica. *J. Mater. Chem. A* **2014**, *2*, 4398–4405.

(11) Ward, T.; Delannoy, L.; Hahn, R.; Kendall, S.; Pursell, C. J.; Louis, C.; Chandler, B. D. Effects of Pd on Catalysis by Au: CO Adsorption, CO Oxidation, and Cyclohexene Hydrogenation by Supported Au and Pd – Au Catalysts. *ACS Catal.* **2013**, *3*, 2644–2653.

(12) Chen, M.; Kumar, D.; Yi, C.; Goodman, D. W. The Promotional Effect of Gold in Catalysis by Palladium-Gold. *Science* **2005**, *310*, 291–294.

(13) Kolli, N. El.; Delannoy, L.; Louis, C. Bimetallic Au–Pd Catalysts for Selective Hydrogenation of Butadiene: Influence of the Preparation Method on Catalytic Properties. *J. Catal.* **2013**, *297*, 79–92.

(14) Qian, K.; Huang, W. Au – Pd Alloying-Promoted Thermal Decomposition of PdO Supported on SiO<sub>2</sub> and Its Effect on the Catalytic Performance in CO Oxidation. *Catal. Today* **2011**, *164*, 320–324.

(15) Shirman, T.; Lattimer, J.; Luneau, M.; Shirman, E.; Reece, C.; Aizenberg, M.; Madix, R.; Aizenberg, J.; Friend, C. M. New Architectures for Designed Catalysts: Selective Oxidation Using AgAu Nanoparticles on Colloid-Templated Silica. *Chem. - Eur. J.* **2018**, *24*, 1833–1837.

(16) Grabar, K. C.; Allison, K. J.; Baker, B. E.; Bright, R. M.; Brown, K. R.; Freeman, R. G.; Fox, A. P.; Keating, C. D.; Musick, M. D.; Natan, M. J. Two-Dimensional Arrays of Colloidal Gold Particles: A Flexible Approach to Macroscopic Metal Surfaces. *Langmuir* **1996**, *12*, 2353–2361.

(17) Ding, Y.; Fan, F.; Tian, Z.; Wang, Z. L. Atomic Structure of Au–Pd Bimetallic Alloyed Nanoparticles. *J. Am. Chem. Soc.* **2010**, *132*, 12480–12486.

(18) Shirman, E.; Shirman, T.; Shneidman, A. V.; Grinthal, A.; Phillips, K. R.; Whelan, H.; Bulger, E.; Abramovitch, M.; Patil, J.; Nevarez, R.; et al. Modular Design of Advanced Catalytic Materials Using Hybrid Organic – Inorganic Raspberry Particles. *Adv. Funct. Mater.* **2017**, No. 1704559.

(19) Ravel, B.; Newville, M. ATHENA, ARTEMIS, HEPHAESTUS: Data Analysis for X-Ray Absorption Spectroscopy Using IFEFFIT. *J. Synchrotron Radiat.* **2005**, *12*, 537–541.

(20) Newville, M.; Ravel, B.; Haskel, D.; Rehr, J. J.; Stern, E. A.; Yacoby, Y. Analysis of Multiple-Scattering XAFS Data Using Theoretical Standards. *Phys. B* **1995**, 208–209, 154–156.

(21) Ankudinov, A. L.; Ravel, B.; Rehr, J. J.; Conradson, S. D. Real-Space Multiple-Scattering Calculation and Interpretation of X-Ray-Absorption near-Edge Structure. *Phys. Rev. B* **1998**, *58*, 7565–7576.

(22) Kresse, G.; Furthmüller, J. Efficient Iterative Schemes for Ab Initio Total-Energy Calculations Using a Plane-Wave Basis Set. *Phys. Rev. B* **1996**, *54*, 11169–11186.

(23) Blöchl, P. E. Projector Augmented-Wave Method. *Phys. Rev. B* **1994**, *50*, 17953–17979.

(24) Kresse, G.; Joubert, D. From Ultrasoft Pseudopotentials to the Projector Augmented-Wave Method. *Phys. Rev. B* **1999**, *59*, 1758–1775.

(25) Perdew, J. P.; Burke, K.; Ernzerhof, M. Generalized Gradient Approximation Made Simple. *Phys. Rev. Lett.* **1996**, *77*, 3865–3868.

(26) Tkatchenko, A.; Scheffler, M. Accurate Molecular Van Der Waals Interactions from Ground-State Electron Density and Free-Atom Reference Data. *Phys. Rev. Lett.* **2009**, *102*, No. 73005.

(27) Methfessel, M.; Paxton, A. T. High-Precision Sampling for Brillouin-Zone Integration in Metals. *Phys. Rev. B* **1989**, *40*, 3616–3621.

(28) Xu, X.; Szanyi, J.; Xu, Q.; Goodman, D. W. Structural and Catalytic Properties of Model Silica-Supported Palladium Catalysts: A Comparison to Single Crystal Surfaces. *Catal. Today* **1994**, *21*, 57–69.

(29) Szanyi, J.; Kuhn, W. K.; Goodman, D. W. CO Oxidation on Palladium. 2. A Combined Kinetic-Infrared Reflection Absorption Spectroscopic Study of Pd(111). *J. Phys. Chem. A* **1994**, *98*, 2978–2981.

(30) Guo, X.; Yates, J. T., Jr. Dependence of Effective Desorption Kinetic Parameters on Surface Coverage and Adsorption Temperature: CO on Pd(111). *J. Chem. Phys.* **1989**, *90*, 6761.

(31) Szanyi, J.; Goodman, D. W. CO Oxidation on Palladium. 1. A Combined Kinetic-Infrared Reflection Absorption Spectroscopic Study of Pd(100). *J. Phys. Chem. A* **1994**, *98*, 2972–2977.

(32) Berlowitz, P. J.; Peden, C. H. F.; Goodman, D. W. Kinetics of CO Oxidation on Single-Crystal Pd, Pt, and Ir. *J. Phys. Chem. A* **1988**, *92*, 5213–5221.

(33) Outka, D. A.; Madix, R. J. The Oxidation of Carbon Monoxide on the Au(110) Surface. *Surf. Sci.* **1987**, *179*, 351–360.

(34) Gottfried, J. M.; Schmidt, K. J.; Schroeder, S. L. M.; Christmann, K. Adsorption of Carbon Monoxide on Au (110) - (1X2). *Surf. Sci.* **2003**, *536*, 206–224.

(35) Kim, J.; Samano, E.; Koel, B. E. CO Adsorption and Reaction on Clean and Oxygen-Covered Au (211) Surfaces. *J. Phys. Chem. B* **2006**, *110*, 17512–17517.

(36) Mcelhiney, G.; Pritchard, J. The Adsorption of Xe and CO on Au(100). *Surf. Sci.* **1976**, *60*, 397–410.

(37) Ruggiero, C.; Hollins, P. Adsorption of Carbon Monoxide on the Gold (332) Surface. *Faraday Trans.* **1996**, *92*, 4829–4834.

(38) Bond, G. C.; Thompson, D. T. Gold-Catalysed Oxidation of Carbon Monoxide. *Gold Bull.* **2000**, *33*, 41–50.

(39) Laoufi, I.; Saint-Lager, M. C.; Lazzari, R.; Jupille, J.; Robach, O.; Garaudée, S.; Cabailh, G.; Dolle, P.; Cruguel, H.; Bailly, A. Size and Catalytic Activity of Supported Gold Nanoparticles: An in Operando Study during CO Oxidation. *J. Phys. Chem. C* **2011**, *115*, 4673–4679.

(40) Timoshenko, J.; Shivhare, A.; Scott, R. W. J.; Lu, D.; Frenkel, A. I. Solving Local Structure around Dopants in Metal Nanoparticles with Ab Initio Modeling of X-Ray Absorption near Edge Structure. *Phys. Chem. Chem. Phys.* **2016**, *18*, 19621–19630.

(41) Paredis, K.; Ono, L. K.; Behafarid, F.; Zhang, Z.; Yang, J. C.; Frenkel, A. I.; Cuenya, B. R. Evolution of the Structure and Chemical State of Pd Nanoparticles during the in Situ Catalytic Reduction of NO with H<sub>2</sub>. *J. Am. Chem. Soc.* **2011**, *133*, 13455–13464.

(42) Frenkel, A. I. Applications of Extended X-Ray Absorption Fine-Structure Spectroscopy to Studies of Bimetallic Nanoparticle Catalysts. *Chem. Soc. Rev.* **2012**, *41*, 8163–8178.

(43) Jentys, A. Estimation of Mean Size and Shape of Small Metal Particles by EXAFS. *Phys. Chem. Chem. Phys.* **1999**, *1*, 4059–4063.

(44) Frenkel, A. I.; Yevick, A.; Cooper, C.; Vasic, R. Modeling the Structure and Composition of Nanoparticles by Extended X-Ray Absorption Fine-Structure Spectroscopy. *Annu. Rev. Anal. Chem.* **2011**, *4*, 23–39.

(45) Frenkel, A. I.; Hills, C. W.; Nuzzo, R. G. A View from the inside: Complexity of the Atomic Scale Ordering in Metal Nanoparticles. *J. Phys. Chem. B* **2001**, *105*, 12689–12703.

(46) Strasser, P.; Koh, S.; Anniyev, T.; Greeley, J.; More, K.; Yu, C.; Liu, Z.; Kaya, S.; Nordlund, D.; Ogasawara, H.; et al. Core – Shell Fuel Cell Catalysts. *Nat. Chem.* **2010**, *2*, 454–460.

(47) Jalan, V.; Taylor, E. J. Importance of Interatomic Spacing in Catalytic Reduction of Oxygen in Phosphoric Acid. *J. Electrochem. Soc.* **1983**, *130*, 2299–2302.

(48) Timoshenko, J.; Wrasman, C. J.; Luneau, M.; Shirman, T.; Cargnello, M.; Bare, S. R.; Aizenberg, J.; Friend, C. M.; Frenkel, A. I. Probing Atomic Distributions in Mono- and Bimetallic Nanoparticles by Supervised Machine Learning. *Nano Lett.* **2019**, *19*, 520–529.

(49) Ozensoy, E.; Goodman, D. W. Vibrational Spectroscopic Studies on CO Adsorption NO Adsorption CO + NO Reaction on Pd Model Catalysts. *Phys. Chem. Chem. Phys.* **2004**, *6*, 3765–3778.

(50) Meier, D. C.; Goodman, D. W. The Influence of Metal Cluster Size on Adsorption Energies: CO Adsorbed on Au Clusters Supported on TiO<sub>2</sub>. *J. Am. Chem. Soc.* **2004**, *126*, 1892–1899.

(51) Yi, C.; Luo, K.; Wei, T.; Goodman, D. W. The Composition and Structure of Pd-Au Surfaces. *J. Phys. Chem. B* **2005**, *109*, 18535–18540.

(52) Stroppa, A.; Kresse, G. The Shortcomings of Semi-Local and Hybrid Functionals: What We Can Learn from Surface Science Studies. *New J. Phys.* **2008**, *10*, No. 063020.

(53) van Spronsen, M. A.; Daunmu, K.; O'Connor, C. R.; Egle, T.; Kersell, H.; Oliver-Meseguer, J.; Salmeron, M. B.; Madix, R. J.; Sautet, P.; Friend, C. M. The Dynamics of Surface Alloys: Rearrangement of Pd/Ag(111) Induced by CO and O<sub>2</sub>. *J. Phys. Chem. C* **2019**, *123*, 8312–8323.

(54) Zhu, B.; Thrimurthulu, G.; Delannoy, L.; Louis, C.; Mottet, C.; Creuze, J.; Legrand, B.; Guesmi, H. Evidence of Pd Segregation and Stabilization at Edges of AuPd Nano-Clusters in the Presence of CO: A Combined DFT and DRIFTS Study. *J. Catal.* **2013**, *308*, 272–281.

(55) Gibson, E. K.; Beale, A. M.; Catlow, C. R. A.; Chutia, A.; Gianolio, D.; Gould, A.; Kroner, A.; Mohammed, K. M. H.; Perdjou, M.; Rogers, S. M.; et al. Restructuring of AuPd Nanoparticles Studied by a Combined XAFS/DRIFTS Approach. *Chem. Mater.* **2015**, *27*, 3714–3720.

(56) Gao, F.; Goodman, D. W. Pd-Au Bimetallic Catalysts: Understanding Alloy Effects from Planar Models and (Supported) Nanoparticles. *Chem. Soc. Rev.* **2012**, *41*, 8009–8020.